Post-Print

Stable sets mapping with Taylor differential algebra with application to ballistic capture orbits around Mars

T. Caleb · G. Merisio · P. di Lizia · F. Topputo

Abstract Ballistic capture orbits offer safer Mars injection at longer transfer time. However, the search for such an extremely rare event is a computationally-intensive process. Indeed, it requires the propagation of a grid sampling the whole search space. This work proposes a novel ballistic capture search algorithm based on Taylor differential algebra propagation. This algorithm provides a continuous description of the search space compared to classical grid sampling research and focuses on areas where the nonlinearities are the largest. Macroscopic analyses have been carried out to obtain cartography of large sets of solutions. Two criteria, named consistency and quality, are defined to assess this new algorithm and to compare its performances with classical grid sampling of the search space around Mars. Results show that differential algebra mapping works on large search spaces, and automatic domain splitting captures the dynamical variations on the whole domain successfully. The consistency criterion shows that more than 87% of the search space is guaranteed as accurate, with the quality criterion kept over 80%.

1 Introduction

Ballistic capture (BC) allows a spacecraft to approach a planet and enter a temporary orbit about it without requiring maneuvers in between. As part of the low-energy transfers, it is a valuable alternative to Keplerian approaches. Exploiting BC grants several benefits in terms of both cost reduction (Belbruno and Miller, 1993) and mission versatility (Belbruno and Carrico, 2000; Topputo and Belbruno, 2015), in general at the cost of longer transfer times (Circi and Teofilatto, 2001; Ivashkin, 2002). In the past, the BC mechanism was used to rescue Hiten (Belbruno and Miller, 1990), and to design insertion trajectories in lunar missions like SMART-1 (Racca et al, 2002) and GRAIL (Chung et al, 2010). In the near future, BepiColombo will exploit BC orbits to be weakly captured by Mercury (Benkhoff et al, 2021; Schuster and Jehn, 2014). BC is an event occurring in extremely rare occasions and requires acquiring a proper state (position and velocity) far away from the target planet (Topputo and Belbruno, 2015). In fact, massive numerical simulations are required to find the specific conditions that support capture (Topputo and Belbruno, 2009) and only approximately 1 out of 10 000 states lead to capture (Luo and Topputo, 2015). In a first effort to reduce the computational burden, the variational theory for

Thomas Caleb (corresponding author)
ISAE-SUPAERO, 10 Avenue Édouard Belin, 54032 - 31055, Toulouse, France
OrcID: 0000-0002-4027-3340
E-mail: thomas.caleb@student.isae-supaero.fr

Gianmario Merisio
Department of Aerospace Science and Technology, Politecnico di Milano, Via La Masa 34, 20156, Milano, Italy
OrcID: 0000-0001-8806-7952
E-mail: gianmario.merisio@polimi.it

Pierluigi di Lizia
Department of Aerospace Science and Technology, Politecnico di Milano, Via La Masa 34, 20156, Milano, Italy
OrcID: 0000-0003-1692-3929
E-mail: pierluigi.dilizia@polimi.it

Francesco Topputo
Department of Aerospace Science and Technology, Politecnico di Milano, Via La Masa 34, 20156, Milano, Italy
OrcID: 0000-0002-5369-6887
E-mail: francesco.topputo@polimi.it

1 Lagrangian coherent structures (Haller, 2011) was recently applied to find BC opportunities more efficiently (Manzi and
2 Topputo, 2021).

3 Differential algebra (DA) propagation is a worthy candidate to reduce the computational burden for the search of BC
4 trajectories. It consists of propagating initial conditions (ICs), not as a single point but as an interval around an IC. Thanks
5 to the Taylor expansions of the flow, the state of any point in the represented interval can be determined through convenient
6 polynomial evaluations (Berz, 1992, 1999). This gain in efficiency comes at the cost of a loss of accuracy due to the finite
7 Taylor expansion. The automatic domain splitting (ADS) algorithm allows to represent large domains accurately when
8 increasing the order of the polynomial expansions fails to do so (Wittig et al, 2015). Indeed, on poorly-defined domains,
9 raising the order will increase the approximation error on the edges while the error will decrease on already well-defined
10 areas. ADS splits the initial domain into smaller sub-domains to reduce the approximation error when it grows above a
11 given tolerance.

12 DA propagation is increasingly used in astrodynamics. Indeed, it provides high performances in uncertainty propagation
13 in the two-body dynamics (Valli et al, 2013), even for highly nonlinear dynamics with large uncertainties when exploiting
14 ADS, as in the case of Apophis (Wittig et al, 2015) or Apollo LM-10 also known as Snoopy (Caleb and Lizy-Destrez,
15 2021). Other applications occur in orbital mechanics, such as propagation of probability density functions (Wittig et al,
16 2017), maximum a posteriori estimation (Servadio et al, 2022), orbit determination (Pirovano et al, 2021; Servadio and
17 Zanetti, 2021), and generation and study of orbit families in the circular restricted three body problem (CR3BP) (Di Lizia
18 et al, 2008; Baresi et al, 2021).

19 DA propagation allows avoiding intensive grid sampling implied by point-wise research of conventional algorithms for
20 designing BC trajectories (Hyeraci and Topputo, 2010; Luo et al, 2014), as it offers a continuous description of the whole
21 search-space. In addition, the computation of a Taylor expansion provides information such as the partial derivatives of
22 the flow up to an arbitrary order (Wittig et al, 2017). Furthermore, the polynomial maps can be manipulated to impose
23 constraints on the flown trajectories (Berz, 1999; Di Lizia et al, 2008).

24 The goal of this work is to use DA mapping to carry out macroscopic analyses of the phase space about Mars to find
25 BC trajectories. Hence, the adaptation of the definition of BC for DA, followed by the definition of two criteria, named
26 consistency and quality, to assess the performances of DA-based mapping of BC compared to point-wise mapping.
27 Cartography of large BC sets about Mars are computed using DA mapping. Mars is chosen without loss of generality
28 due to its relevance in the long-term exploration. The work proposes an alternative classification algorithm to sort the
29 sub-domains produced by the ADS algorithm in newly defined capture sets. While DA mapping allows performing good
30 macroscopic cartography of the search space, it does not allow to fully replace point-wise mapping. However, DA mapping
31 has the advantage of being continuous, so meaning that the behavior of any point in the search space is defined. On the
32 contrary, a point-wise mapping delivers precise knowledge on the discrete set of propagated ICs only. As a consequence,
33 the behavior of the continuous space between two points is unknown and can be challenging to interpolate due to the
34 nonlinear dynamics.

35 The remainder of the paper is organized as follows. In Section 2, the dynamical model employed is introduced, as well
36 as the weak stability boundary (WSB) concept, the BC mechanism, and the DA propagation. Then, the description of
37 the characterization process, and the mapping-assessment methodology follow in Section 3. Results are presented and
38 discussed in Section 4. Eventually, conclusions are drawn in Section 5 together with the presentation of future work.

2 Background

40 Details about dynamical model, WSB, BC phenomenon, DA propagation, and ADS algorithms are herewith presented.

41 2.1 Dynamical model

42 According to the nomenclature introduced in Luo et al (2014), a *target* (also referred to as *central body*) and a *primary*
43 are defined. The target being the body around which the motion of the spacecraft is studied (Mars in this work), and the
44 primary being the body around which the target revolves (the Sun). Target and primary masses are m_t and m_p, respectively.

45 *2.1.1 Reference frames*

46 In this work, the following reference frames are used: J2000, and RTN@t_i.

47 *J2000.* Defined on the Earth's mean equator and equinox, the J2000 is an inertial frame determined from observations of
48 planetary motions which was realized to coincide almost exactly with the International Celestial Reference Frame (ICRF)
49 (Archinal et al, 2011). Equations of motion (EoM) are integrated in this reference frame.

Table 1: Assumed spacecraft specifications.

Specification	Symbol	Value
Mass	m	24 kg
SRP area	A	0.32 m^2
Coefficient of reflectivity	C_r	1.3

1 *RTN@t_i.* The radial-tangential-normal of date frame (RTN@t_i) is an inertial frame frozen at a prescribed epoch t_i. The
2 frame is centered at the target. The *x*-axis is aligned with the primary–secondary direction, the *z*-axis is normal to the
3 primary–secondary plane in the direction of their angular momentum, and the *y*-axis completes the dextral orthonormal
4 triad. ICs are defined in this frame (Luo and Topputo, 2015).

5 *2.1.2 Ephemerides*

6 Precise states of the Sun and the major planets are retrieved from the Jet Propulsion Laboratory (JPL)'s planetary
7 ephemerides `de440s.bsp`[1] (or DE440s) (Park et al, 2021). Additionally, the ephemerides `mars097.bsp` of Mars (the
8 target) and its moons are employed[2]. The following generic leap seconds kernel (LSK) and planetary constants kernel
9 (PCK) are used: `naif0012.tls`, `pck00010.tpc`, and `gm_de431.tpc`[3].

10 *2.1.3 Equations of motion*

11 The EoM used are those of the restricted *N*-body problem. The gravitational attractions of the Sun, Mercury, Venus,
12 Earth (B[4]), Mars (central body), Jupiter (B), Saturn (B), Phobos, and Deimos are considered. Additionally, solar
13 pressure (SRP) is also included and implemented as a *cannonball* or *spherical* model (Scheeres et al, 2011). The assumed
14 spacecraft specifications needed to evaluate the SRP perturbation are collected in Table 1. They are compatible with the
15 specifications of a 12U deep-space CubeSat (Topputo et al, 2021).

16 The EoM, written in a non-rotating Mars-centered reference frame are (Luo et al, 2014; Merisio and Topputo, 2021)

$$\ddot{\mathbf{r}} = -\frac{\mu_t}{r^3}\mathbf{r} - \sum_{i\in\mathbb{P}}\mu_i\left(\frac{\mathbf{r}_i}{r_i^3} + \frac{\mathbf{r}-\mathbf{r}_i}{\|\mathbf{r}-\mathbf{r}_i\|^3}\right) + \frac{QA}{m}\frac{\mathbf{r}-\mathbf{r}_\odot}{\|\mathbf{r}-\mathbf{r}_\odot\|^3} \tag{1}$$

17 where μ_t is the gravitational parameter of the target body; $\mathbf{r}$ is the position vector of the spacecraft with respect to the
18 target and r is its magnitude; $\mathbb{P}$ is a set of $N-2$ indexes each referring to a perturbing body; μ_i and $\mathbf{r}_i$ are the gravitational
19 parameter and position vector with respect to the target of the *i*-th body, respectively; A is the Sun-projected area on the
20 spacecraft for SRP evaluation; m is the spacecraft mass; $\mathbf{r}_\odot$ is the position vector of the Sun with respect to the target.
21 Lastly, Q is equal to

$$Q = \frac{LC_r}{4\pi c} \tag{2}$$

22 where C_r is the spacecraft coefficient of reflectivity, $c = 299\,792\,458\,\text{m s}^{-1}$ taken from SPICE (Acton, 1996; Acton et al,
23 2018) is the speed of light in vacuum, and $L = S_\odot 4\pi d_{\text{AU}}^2$ is the luminosity of the Sun. The latter is computed from the solar
24 constant[5] $S_\odot = 1367.5\,\text{W m}^{-2}$ evaluated at $d_{\text{AU}} = 149\,597\,870\,613.6889\,\text{m}$ corresponding to 1 AU according to SPICE
25 (Acton, 1996; Acton et al, 2018).

26 *2.1.4 Numerical integration of EoM*

27 The EoM in Eq. (1) are integrated in their nondimensional form to avoid ill-conditioning (Luo et al, 2014). Nondi-
28 mensionalization units are reported in Table 2. For point-wise simulations, the numerical integration is carried with
29 the Dormand-Prince 8th-order embedded Runge-Kutta method (DOPRI8) propagation scheme (Montenbruck and Gill,
30 2000). It is an adaptive step, 8th-order Runge-Kutta (RK) integrator with 7th-order error control, the coefficients were
31 derived by Prince and Dormand (Prince and Dormand, 1981). As for the DA simulations, the propagation scheme is
32 Dormand-Prince of order 8(5,3) embedded Runge-Kutta method (DOP853) (Hairer et al, 1993), which is of the same
33 8th-order RK integrator family. However, the error control is performed with a 3rd-order and a 5th-order estimation. The
34 dynamics are propagated setting the relative tolerance to 10^{-12} (Luo et al, 2014).

---

[1] Data publicly available at: `https://naif.jpl.nasa.gov/pub/naif/generic_kernels/spk/planets/de440s.bsp` [retrieved Feb 1, 2022].

[2] `~/spk/satellites/mars097.bsp` [retrieved Feb 1, 2022].

[3] Data publicly available at: `https://naif.jpl.nasa.gov/pub/naif/generic_kernels/lsk/naif0012.tls`, `~/generic_kernels/pck/pck00010.tpc`, and `~/generic_kernels/pck/gm_de431.tpc` [retrieved Feb 1, 2022]. The `gm_de431.tpc` PCK kernel is used because the new version consistent with the ephemerides DE440s has not been released yet.

[4] Here B stands for barycenter.

[5] `https://extapps.ksc.nasa.gov/Reliability/Documents/Preferred_Practices/2301.pdf` [last accessed Feb 1, 2022].

Table 2: Nondimensionalization units.

Unit	Symbol	Value	Comment
Gravity parameter	MU	$42\,828.376\,\text{km}^3\,\text{s}^{-2}$	Mars' gravity parameter μ_t
Length	LU	$3396.0000\,\text{km}$	Mars' radius $R_{\male}$
Time	TU	$956.281\,42\,\text{s}$	$(\text{LU}^3/\text{MU})^{0.5}$
Velocity	VU	$3.551\,255\,8\,\text{km}\,\text{s}^{-1}$	LU/TU

2.2 Weak stability boundary and ballistic capture mechanism

Over the years, the WSB was defined in many different ways. It was initially identified as a fuzzy boundary region placed at approximately 1.5×10^6 km from the Earth in the Sun–Earth direction (Belbruno, 1987; Belbruno and Miller, 1990). An algorithmic definition followed in Belbruno (2004), later extended in García and Gómez (2007), Topputo and Belbruno (2009), and Sousa Silva and Terra (2012). Then, the WSB was interpreted as the intersection of three sub-sets of the phase space (Topputo et al, 2008; Belbruno et al, 2008). The WSB concept being closely connected to BC (Belbruno, 2004), a formal definition and a methodology for its derivation from weakly stable and unstable sets were finally proposed in Hyeraci and Topputo (2010). To date, despite the effort put in numerous works (García and Gómez, 2007; Topputo et al, 2008; Belbruno et al, 2008, 2010, 2013), both WSB and BC are still not completely understood. Nonetheless, a connection between celestial and quantum mechanics was recently found exploiting the WSB (Belbruno, 2020), providing a fresh perspective to tackle the problem.

BC orbits are characterized by ICs escaping the target when integrated backward and performing n revolutions about it when propagated forward, neither impacting or escaping the target. In forward time, particles flying on BC orbits approach the target coming from outside its sphere of influence and remain temporarily captured about it. After a certain time, the particle escapes if an energy dissipation mechanism does not take place to make the capture permanent. To dissipate energy either a breaking maneuver or the target's atmosphere (if available) could be used (Luo and Topputo, 2021). In this work, BC sets for comparison purposes are derived propagating the EoM in Eq. (1) and following the procedure in Luo et al (2014).

When searching for BC opportunities, most of the trajectories found are spurious solutions which are typically not useful for mission design purposes (Luo et al, 2014). Useful solutions are detected exploiting the regularity index[1] S and regularity coefficient $\Delta S_\%$ (Dei Tos et al, 2018). The aim is seeking for ideal orbits that presents regular post-capture legs resulting in n revolutions about the target which are similar in orientation and shape. Numerical experiments showed that high-quality post-capture orbits are identified by small regularity index and coefficient (Dei Tos et al, 2018; Luo and Topputo, 2017, 2015; Luo et al, 2014). If the regularity index and coefficient are indicators used to qualitatively judge post-capture legs, capture occurrence is quantitatively measured through the capture ratio $\mathcal{R}_\mathcal{C}$ (Luo and Topputo, 2015). Typically, search spaces characterized by larger capture ratio are desirable when looking for BC orbits.

Effects on BC by gravitational attractions of many bodies besides the primaries and SRP have been investigated in previous works (Merisio and Topputo, 2021; Aguiar and Topputo, 2018; Luo and Topputo, 2017, 2015), with Merisio and Topputo (2021), and Aguiar and Topputo (2018) also considering the target non-spherical gravity perturbations. Compared to the restricted three-body problem, the N-body model is more adequate for constructing ballistic capture orbits as proved in Luo and Topputo (2015), with a particle being more easily captured when considering additional gravitational attractions. The latter was later confirmed in Luo and Topputo (2017), where the presence of moons is demonstrated to increase the capture ratio $\mathcal{R}_\mathcal{C}$ and improves the regularity of post-capture orbits while accommodating larger pre-capture energies. Similarly, SRP increases the chances of being temporarily captured about the target and regularizes the post-capture legs (Merisio and Topputo, 2021; Aguiar and Topputo, 2018). Even if not duly discussed, the aforementioned remarks are observed also in the results of this work. Overall, supplementary terms in the dynamics seem to favor the manifestation of the BC phenomenon.

2.2.1 Definitions of particle stability and sub-sets

A particle stability is inferred using a plane in the three-dimensional physical space (Belbruno and Miller, 1993), according to the spatial stability definition provided in Luo et al (2014). The following indications are used to classify stability, see Luo et al (2014) for more details: 1) a particle completes a revolution around the target according to *Remark 1* and Eq. (5) in Luo et al (2014); 2) a particle escapes from the target according to *Remark 2* and Eq. (6) in Luo et al (2014); 3) a particle impacts with the target according to *Remark 3* and Eq. (7) in Luo et al (2014). Consistent variants of Eq. (7) in Luo et al (2014) can be derived to locate impacts with target's moons, if present.

---

[1] In previous works this was referred to as stability index (Luo et al, 2014; Luo and Topputo, 2015, 2017). However, in Dei Tos et al (2018), the adjustment from *stability* to *regularity* index was proposed to avoid misunderstandings with the periodic orbit stability index. The same nomenclature introduced in Dei Tos et al (2018) is used in this work.
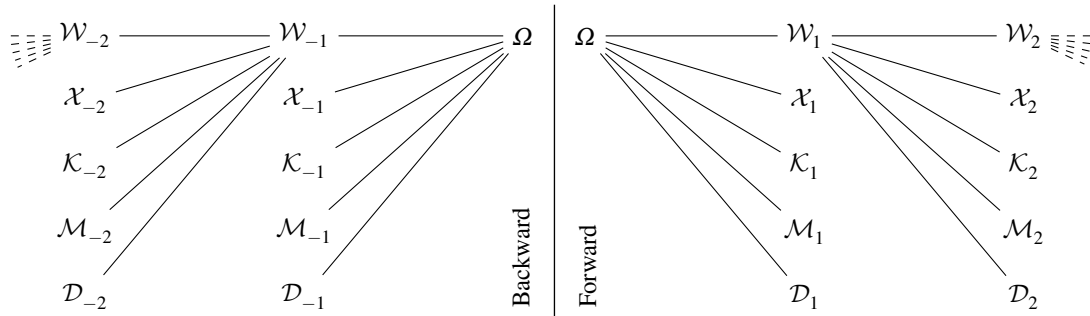
Fig. 1: Sets relations according to the algorithmic definition of WSB.

1 Based on its dynamical behavior, a propagated trajectory is said to be: i) *weakly stable* (sub-set $\mathcal{W}_i$) if the particle performs
2 i complete revolutions around the target without escaping or impacting with it or its moons; ii) *unstable* (sub-set $\mathcal{X}_i$) if the
3 particle escapes from the target before completing the i-th revolution; iii) *target–crash* (sub-set $\mathcal{K}_i$) if the particle impacts
4 with the target before completing the i-th revolution; iv) *moon–crash* (sub-set $\mathcal{M}_i$) if the particle impacts with one of the
5 target's moons before completing the i-th revolution; v) *acrobatic* (sub-set $\mathcal{D}_i$) if none of the previous conditions occurs
6 within the integration time span. Conditions ii)-v) apply after the particle performs $(i-1)$ revolutions around the target.
7 The sub-sets are defined for $i \in \mathbb{Z} \setminus \{0\}$, where the sign of i informs on the propagation direction. When $i > 0$ ($i < 0$)
8 the IC is propagated forward (backward) in time. The overall domain, union of all sub-sets, is defined as Ω. A graph
9 clarifying the relations between sub-sets is shown in Fig. 1. A capture set is defined as $\mathcal{C}^n_{-1} := \mathcal{W}_n \cap \mathcal{X}_{-1}$. Therefore, it is
10 the intersection between the stable set in forward time $\mathcal{W}_n$ and the unstable set in backward time $\mathcal{X}_{-1}$ (Luo et al, 2014).

2.3 Differential algebra

12 DA propagation consists of assimilating a function f of v variables, contained in C^{k+1}, with $T_f^{(k)}$ the Taylor expansion of f
13 at order k (Berz, 1999). The computation of such polynomials can be performed efficiently, and provides a representation
14 of the function f on all of its domain. Moreover, the DA structure ensures that algebraic and functional operations are
15 well-defined, particularly for the numerical solving of ordinary differential equations (Berz, 1992).

16 The main advantage of this method is that the polynomial map only needs to be computed once, and then it is evaluated
17 in an arbitrarily large number of points. In other words, to perform a Monte-Carlo estimation with a sample of size S,
18 only one computation of the map is needed, followed by S polynomial evaluations, while classic Monte-Carlo requires S
19 propagations, see Armellin et al (2010). The DA engine used in this work is the differential algebra core engine (DACE)[1],
20 implemented by Politecnico di Milano (Rasotto et al, 2016; Massari et al, 2018).

2.3.1 Automatic domain splitting

22 DA propagation allows reducing the approximation error by increasing the order k of the polynomial mapping. Nevertheless,
23 increasing the order leads to an important growth of the computational time. Thus, the introduction of ADS, see Wittig
24 et al (2015), and Pirovano et al (2021) for more details.

25 The farther a point is from the constant part of the Taylor expansion, the higher the loss of accuracy. The ADS algorithm
26 controls this error by dividing the domain into halves until the accuracy is below a predetermined tolerance. Therefore,
27 each new sub-domain is represented by its polynomial map causing a much smaller approximation error, at a controlled
28 computational cost (Wittig et al, 2015). The ADS creates a division of the initial domain separating areas with different
29 behaviors from one another. The ADS algorithm requires the passing of two parameters, in addition to the order of the DA:
30 the tolerance, and the maximum number of splits allowed. The former being the approximation error threshold before the
31 splitting of a domain occurs, while the latter being the number of times the ADS routine can be applied to a sub-domain.

3 Methodology

33 To map BC sets on the search space using DA propagation, a novel classification algorithm is devised and herewith
34 presented. To be successful, the algorithm requires an accurate revolution period estimation. Consistency and quality
35 criteria are defined to evaluate performances of the resulting mapping. Finally, fresh representation methods to visualize
36 properly the large resulting amount of data are exposed.

---

[1] Library available at: https://github.com/dacelib/dace [last accessed Feb 1, 2022].
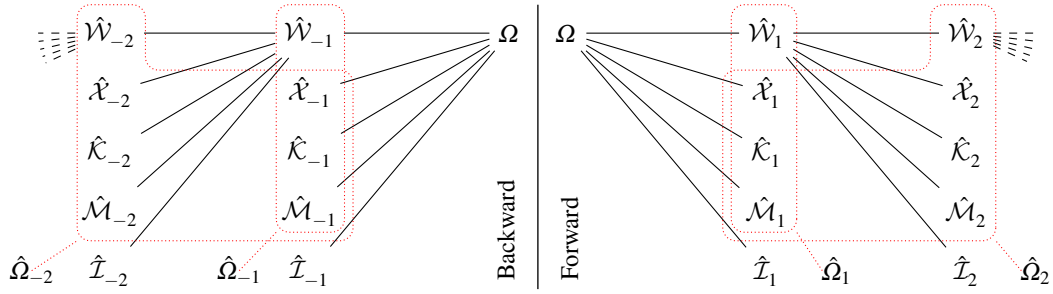
Fig. 2: Sets relations according to classification with DA and ADS.

1   The search space is chosen to maximize the capture ratio $\mathcal{R}_c$ based on the analysis reported in Luo and Topputo (2015). It
2   is defined in the Mars-centered RTN reference frame at capture epoch t_0 on December 9, 2023, at 00:45:18.363 (UTC). At
3   that epoch, Mars's true anomaly with respect to the Sun is equal to 270 deg, maximizing $\mathcal{R}_c$ (Luo and Topputo, 2015). The
4   selected plane is defined by inclination $i = 0.6283\,\text{rad}$, and right ascension of the ascending node RAAN $= 0.6283\,\text{rad}$.
5   That because, according to Fig. 10 in Luo and Topputo (2015), such values maximize the capture ratio for Mars. Sought
6   trajectories have osculating eccentricity $e = 0.99$ (Topputo and Belbruno, 2015), and mean anomaly $M = 0\,\text{rad}$ at the
7   initial epoch t_0. If $R_{\male}$ is the radius of Mars in km, then the search space on the plane defined above is a circular crown
8   centered at Mars, from radius $R_{\male} + 100\,\text{km}$ up to radius $5R_{\male}$. Hence,

$$(r_p, \omega) \in \left[R_{\male} + 100\,\text{km}, 5 \cdot R_{\male} \right] \times (-\pi, \pi] \tag{3}$$

9   with r_p the radius of the periapsis, and ω the argument of the periapsis.

10   The main difference between the point-wise mapping of sets performed by GRAvity TIdal Slide (GRATIS) (Topputo
11   et al, 2018) and the DA mapping presented in this work is that the DA propagator does not allow to count revolutions.
12   It means the sub-domains cannot be classified in the sub-sets defined in Section 2.2.1. New sets are defined to solve
13   this problem. Furthermore, instead of tracking revolutions geometrically, as in Luo et al (2014), the proposed novel
14   classification algorithm counts revolution periods. Finally, a bridge between the two mapping methods is established.

15   3.1 Redefinition of sub-sets and classification algorithm

16   There is no direct method to use the definitions of Section 2.2.1 with DA. This is because accurately counting the
17   revolutions of a continuous set of particles around the target cannot be performed as in *Remark 1* and Eq. (5) in Luo
18   et al (2014). Instead of using this condition to count completed revolutions, the number of period elapsed since epoch is
19   used. Consequently, $\mathcal{D}_i$ cannot be defined when using DA propagation. Moreover, if a subdomain reached the minimum
20   size allowed by the ADS algorithm, and it tries to split again, the accuracy of the mapping of this sub-domain cannot be
21   guaranteed. Thus, these inconsistent sub-domains need to be ruled out from the sub-sets, so that only the consistent ones
22   are retained.

23   Therefore, the definitions of Section 2.2.1 are adapted to DA propagation as follows: i) *inconsistent* (sub-set $\hat{\mathcal{I}}_i$) if the
24   sub-domain performed the maximum number of splits allowed and tries to split again before completing the i-th period;
25   ii) *weakly stable* (sub-set $\hat{\mathcal{W}}_i$) if the sub-domain is consistent, and performs i complete periods without escaping or
26   impacting the target or its moons; iii) *unstable* (sub-set $\hat{\mathcal{X}}_i$) if the sub-domain is consistent, and escapes from the target
27   before completing the i-th; iv) *target–crash* (sub-set $\hat{\mathcal{K}}_i$) if the sub-domain is consistent, and impacts with the target
28   before completing the i-th period; v) *moon–crash* (sub-set $\hat{\mathcal{M}}_i$) if the sub-domain is consistent, and impacts with one of
29   the target's moons before completing the i-th period. Conditions i), and ii)-v) apply after the particle performs $(i-1)$
30   periods around the target. As in Section 2.2.1, the sub-sets are defined for $i \in \mathbb{Z} \setminus \{0\}$ and the same considerations about
31   propagation direction still apply. Moreover, the domain that is consistent after i periods is defined as

$$\hat{\Omega}_i = \Omega \setminus \bigcup_{j=1}^{|i|} \hat{\mathcal{I}}_{\text{sgn}(i)j}. \tag{4}$$

32   In Fig. 2, a graph reporting the relations between the sub-sets adapted to DA propagation is shown. As usual, a capture set
33   is defined in DA propagation as $\hat{\mathcal{C}}_{-1}^n := \hat{\mathcal{W}}_n \cap \hat{\mathcal{X}}_{-1}$.

34   3.2 Classification algorithm

35   The classification algorithm shown in Algorithm 1 is a while loop divided in two parts:

Algorithm 1: Classification algorithm.

Set either $i = 1$ (forward propagation) or $i = -1$ (backward propagation);

Set the search space $\hat{\mathcal{W}}_0 = \Omega$;

Set capture epoch $T_0 = t_0$;

Set maximum number of periods $n_{\max}$;

while $|i| \leq n_{\max}$ **do**

    Propagate $\hat{\mathcal{W}}_{i-\mathrm{sgn}(i)}$ from $T_{i-\mathrm{sgn}(i)}$ to T_i;

    Extract inconsistent sub-domains in $\hat{\mathcal{I}}_i$;

    Extract crash sub-domains in $\hat{\mathcal{K}}_i$;

    Extract moon-crash sub-domains in $\hat{\mathcal{M}}_i$;

    Extract escaped sub-domains in $\hat{\mathcal{X}}_i$;

    Retain remaining sub-domains as $\hat{\mathcal{W}}_i$;

    Set $i = i + \mathrm{sgn}(i)$;

end

---

1. the DA propagation of the stable set $\hat{\mathcal{W}}_{i-1}$ from the current period to the next one, thus from T_{i-1} to T_i;

2. the extraction of all the sub-domains to classify them in the right set.

A bridge is built between the definitions of Section 2.2.1 and the ones of Section 3.1. The similarities are

$$\hat{\Omega}_i \to \Omega, \quad \hat{\mathcal{I}}_i \to \emptyset, \quad \hat{\mathcal{K}}_i \to \mathcal{K}_i, \quad \hat{\mathcal{M}}_i \to \mathcal{M}_i, \quad \hat{\mathcal{X}}_i \to \mathcal{X}_i, \quad \hat{\mathcal{W}}_i \to \mathcal{W}_i, \quad \hat{\mathcal{C}}_{-1}^i \to \mathcal{C}_{-1}^i, \quad \emptyset \to \mathcal{D}_i. \tag{5}$$

Note that the inconsistent set $\hat{\mathcal{I}}_i$ is mapped to the empty set due to the inability to compute these sub-domains with accuracy. Moreover, the acrobatic set $\mathcal{D}_i$ is not mapped by the DA classification algorithm. Nonetheless, this region of the search space represents a small fraction of the total for long enough propagation times (Luo et al, 2014).

3.3 Propagation time span

Since it is not possible to track revolutions geometrically, they are tracked by counting the revolution periods. Thus, the need to estimate them with fidelity. These periods are determined by a least-square regression on data from point-wise computations issued by GRATIS[1], with respect to the radius of the periapsis r_p. Two regression shapes are chosen:

1. a square root shape

$$T_{\sqrt{\cdot}} = A + B\sqrt{r_p}, \text{ with } A = -0.19329, \ B = 2.10555; \tag{6}$$

2. a logarithmic shape

$$T_{\ln(\cdot)} = A + B\ln(r_p), \text{ with } A = -7.35410, \ B = 1.44254. \tag{7}$$

Fig. 3 shows these regressions for 2 and 6 periods, compared to the dataset generated by GRATIS.

For the rest of this work, the logarithmic shape is chosen over the square root one, due to a better fit. Nevertheless, the regression does not fit well for 2 revolutions at large r_p, due to the high concentration of points at small radii, as shown by Fig. 4. Moreover, Fig. 5 highlights how the distribution of the revolution times is widely spread, with respect to r_p, as the whiskers represent the minimum and maximum values, with the median in the middle. Therefore, the regressions displayed in Eqs. (6) and (7) make up for a strong hypothesis on the behavior on the revolution periods.

3.4 Consistency and quality criteria

Once the classification of the search space is performed, tools need to be developed to evaluate it. Two criteria are defined to do so. The first is the *consistency* criterion, which assesses the parts of the domain where the DA mapping cannot be trusted. The second is the *quality* criterion, which assesses the performances of the DA mapping with respect to point-wise reference mapping carried out with GRATIS.

---

[1] The time regressions have been derived from ICs propagated taking into account also the gravitational attractions of Uranus (B), and Neptune (B), later discarded due to their negligible influence.
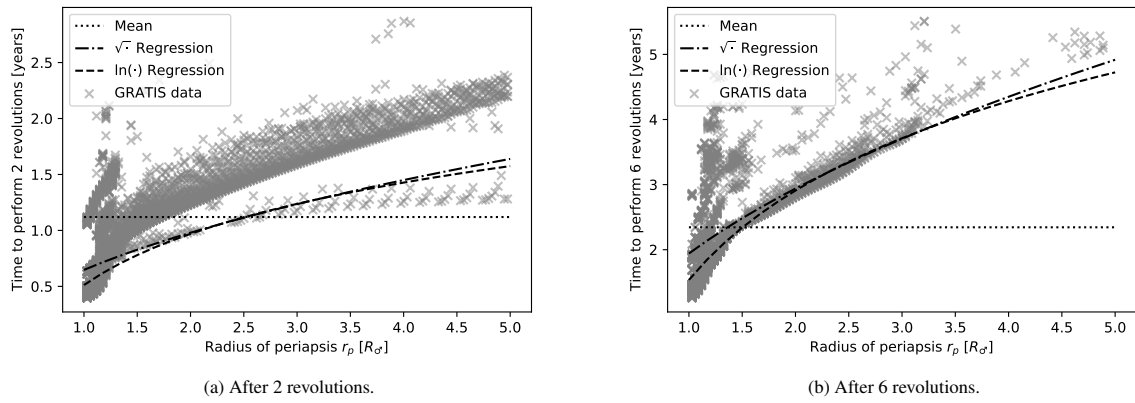
(a) After 2 revolutions.

(b) After 6 revolutions.

Fig. 3: Regression of the revolution periods as a function of the radius of the periapsis r_p. Data from point-wise computations issued by GRATIS.
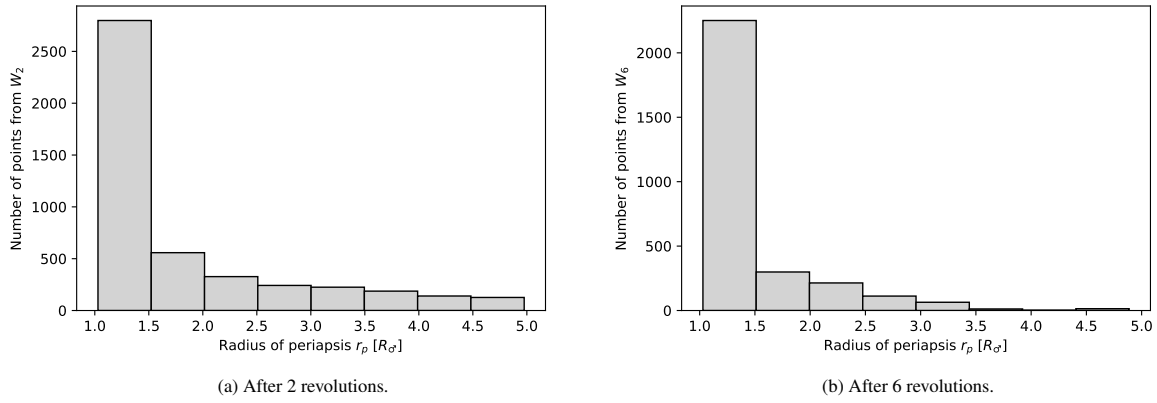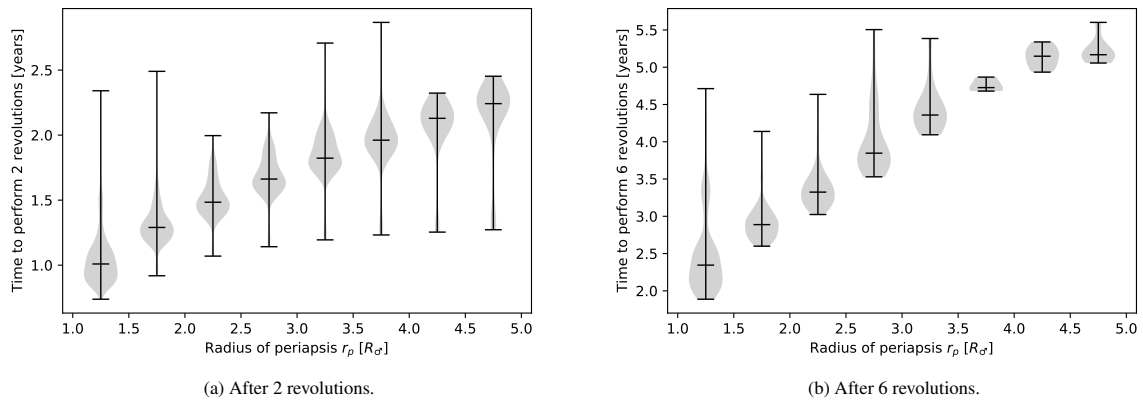

(a) After 2 revolutions.

(b) After 6 revolutions.

Fig. 4: Histogram of the periapsis r_p. Data from point-wise computations issued by GRATIS.

(a) After 2 revolutions.

(b) After 6 revolutions.

Fig. 5: Distribution of the revolution periods as a function of the radius of the periapsis r_p. Data from point-wise computations issued by GRATIS.

Consistency criterion. The consistency is a number assigned to each sub-domain. After the classification algorithm is performed, each sub-domain is given a consistency of either 1 if it does not belong to an inconsistent set $\hat{\mathcal{I}}_i$, or 0 if it does. Consequently, the default consistency of a sub-domain is 1. Yet, if a sub-domain reaches the minimum size allowed and tries to split again, it is set to 0. The main interest is to compute the global consistency on all of the search space. It can be computed by performing the mean of the consistencies, pondered by the size of each sub-domain. The global consistency will then represent the ratio of the mapping that is not inconsistent. Therefore, it is the proportion of the mapping where ADS guarantees the accuracy of the mapping.
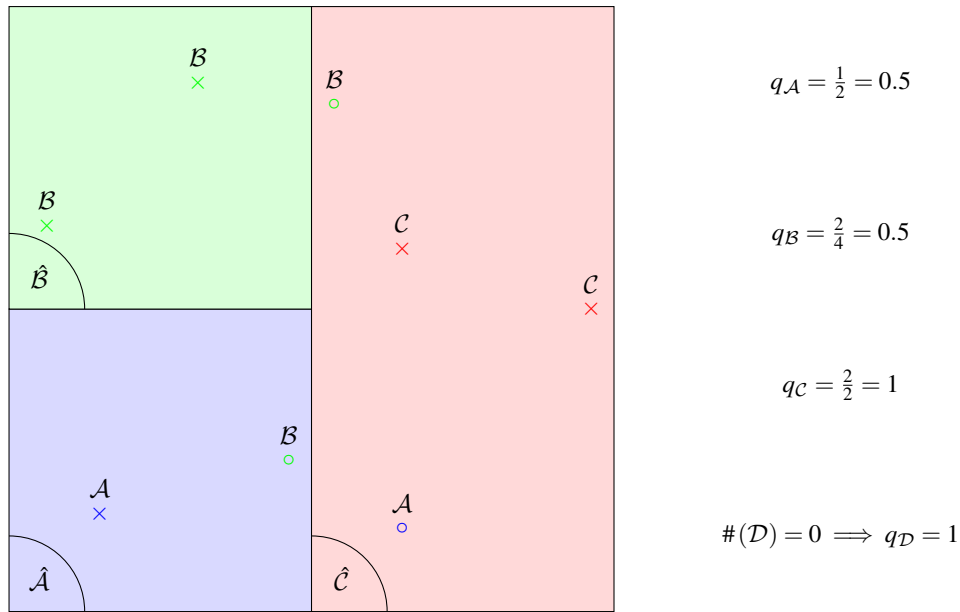
Legend:

Sub-domain classified by DA

×   GRATIS IC accurately mapped by DA

○   GRATIS IC inaccurately mapped by DA

Fig. 6: Example of computation of the quality criterion for a given mapping.

Quality criterion. The quality criterion is a value assigned to each set issued from GRATIS's classification. It represents the proportion of the set from GRATIS that is well-mapped by the DA classification algorithm. To be computed, the quality criterion requires a sample propagated point-wise with GRATIS. The quality $q_{\mathcal{A}}$ of a GRATIS set $\mathcal{A}$ is computed as follows:

1. for each point $x \in \mathcal{A}$, if x belongs to the set $\hat{\mathcal{A}}$, according to the bridge between DA and point-wise classification exposed in Eq. (5), then the quality of that point $q_x = 1$, otherwise $q_x = 0$;

2. the quality $q_{\mathcal{A}}$ of a set $\mathcal{A}$ is the mean of all the values of $(q_x)_{x \in \mathcal{A}}$. In other words

$$q_{\mathcal{A}} = \frac{\#\left(\mathcal{A} \cap \hat{\mathcal{A}}\right)}{\#(\mathcal{A})}. \tag{8}$$

In the case where $\#(\mathcal{A}) = 0$, then $\#\left(\mathcal{A} \cap \hat{\mathcal{A}}\right) = 0$. Thus, by convention $q_{\mathcal{A}} = 1$;

3. the confidence intervals on $q_{\mathcal{A}}$ are evaluated according to Robert and Casella (2004), and Hanley and Lippman-Hand (1983).

The quality represents the probability for a point from the point-wise mapping to be mapped correctly with the DA mapping. Note that since $\hat{\mathcal{I}}_i$ is mapped to $\emptyset$, the quality criterion of Ω_i is less than or equal to the consistency criterion after i revolutions. A schematic representation clarifying the meaning of the quality criterion is shown in Fig. 6.

3.5 Representation methods

The representation of the results produced by this methodology raises two issues. Firstly, due to ADS, the largest fully-split sub-domains have a size of $\approx 50\,\mathrm{km}$, while the typical length of the search space is $\approx 3000\,\mathrm{km}$. Thus, it is impossible to see them or smaller sub-domains on a global representation. To solve this problem, the resolution of the display is downgraded to a smaller one. Furthermore, instead of plotting each sub-domain independently, the density of sub-domains per pixel is preferred. It allows detecting areas with a high number of sub-domains even on a global visualization.

Secondly, the Cartesian representation of the search space tends to shrink details for low values of the radius of the periapsis r_p, while the size of structures located at larges values of r_p is amplified. However, areas with a larger amount of

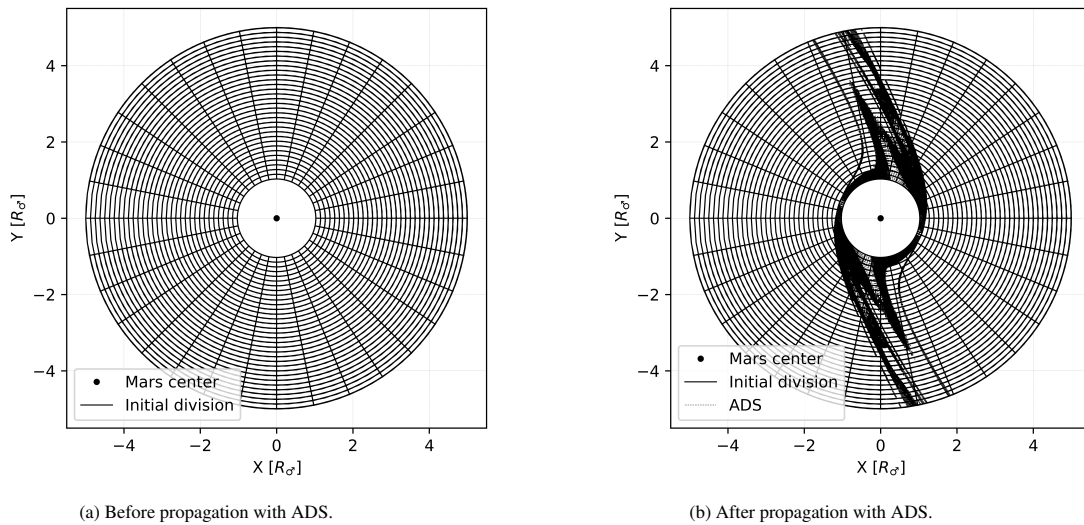(a) Before propagation with ADS.

(b) After propagation with ADS.

Fig. 7: Cartesian visualization of the mapping of the search space.

data to visualize are located at small r_p. Thus, results are visualized on the $r_p \times \omega$ plane, which is the search space in Keplerian coordinates.

4 Results

In this work, the results from two simulations with initial grids having different resolution are presented. The order of the DA mappings is 20 to provide good accuracy on consistent domains and delay the triggering of ADS. Therefore, increasing the order lowered the computational time and enhanced consistency. Nevertheless, a larger order would not increase the approximation performances, see Wittig et al (2015). The first simulation relies on a coarse grid providing a low-resolution mapping where the search space is initially divided into 32×32 domains and the maximum number of splits allowed to the ADS algorithm is 9. On the contrary, the second is computed on a finer grid returning a high-resolution mapping. In the latter, the search space is divided into 128×128 domains and 10 maximum splits are allowed. Results are visualized in the low-resolution mapping in Cartesian coordinates. Sub-domains densities and last step epochs are computed on the whole search space. Then, the DA classification outcome is rendered for qualitative analysis. Finally, a quantitative analysis of those mappings exploiting consistency and quality criteria follows.

4.1 Mapping

Fig. 7 represents the low-resolution search space in Cartesian coordinates, before and after the propagation with ADS (left and right, respectively). Before propagation, the search space is divided regularly into small domains for parallelization (see Fig. 7a). Conversely, an irregular sub-divisions highlighting dynamical changes is shown in Fig. 7b. This visualization shows the necessity to use different visualization methods. Indeed, it is hard to analyze close to zones where ADS creates a large number of domains, although these are the most interesting regions.

4.1.1 Density of sub-domains and last step epochs

Fig. 8 shows the density of sub-domains for the low-resolution and high-resolution mappings (left and right, respectively). They mostly differ because the high-resolution mapping provides more variations. Indeed, the density is either maximal (in grey) or minimal (in white) in the low-resolution one. On the contrary, the high-resolution mapping provides more shades, highlighting several degrees of nonlinearity accurately mapped. In addition, the low-resolution mapping created 7.2×10^4 sub-domains. It is fewer propagations than the point-wise cartography of Section 4.1.2 for the representation of the same search space. Meanwhile, the number of sub-domains in the high-resolution mapping is 1.2×10^6, thus, more than ten times the number of point-wise propagations. Therefore, there is no computational benefit in using high-resolution mapping instead of point-wise propagations. However, as opposed to a point-wise mapping, the sub-domains are heterogeneously distributed, and are mainly located in highly nonlinear regions. For instance, the vicinity of Mars and areas that lead to collisions have a large sub-domains density compared to the majority of the search space. Furthermore, the sub-domain density draws the boundaries between different sets, due to their different dynamical behaviors. On that

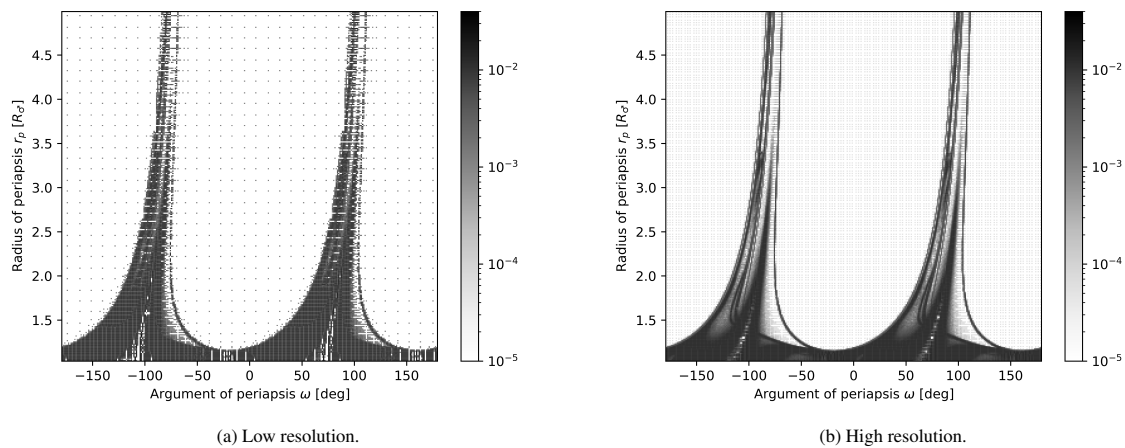(a) Low resolution.

(b) High resolution.

Fig. 8: Density of sub-domains, in percent of the overall sum of sub-domains after 6 periods.
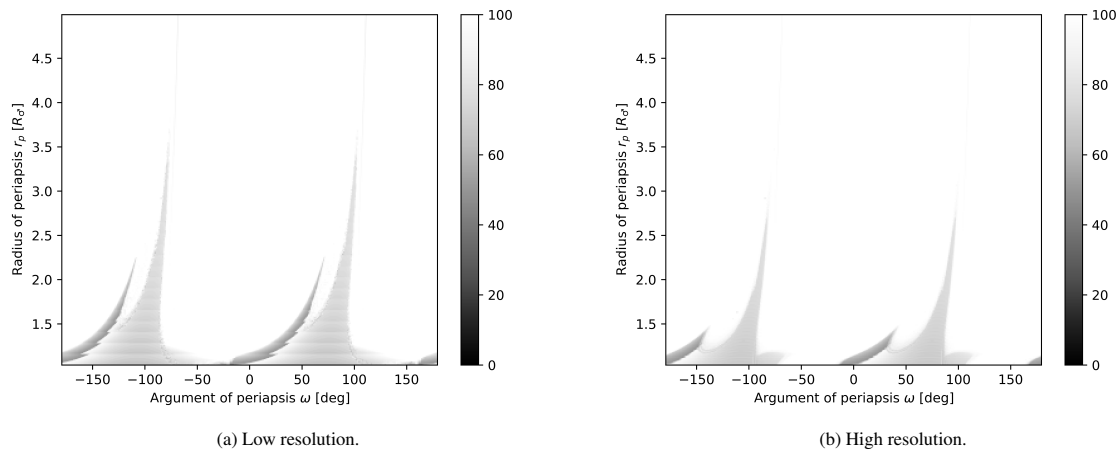

(a) Low resolution.

(b) High resolution.

Fig. 9: Last step epochs, in percent of the overall propagation time span corresponding to 6 periods.

account, DA mapping provides useful macroscopic information on the search space, while grid point-wise mapping does not allow highlighting highly nonlinear areas or boundaries.

Moreover, epochs of last steps carried out by the propagation scheme are shown in Fig. 9, in percent of the overall propagation time span. The integration of a sub-domain stops either after a collision occurs or when the sub-domain itself is declared inconsistent. Note that at low r_p, the lightest zones on the low-resolution mapping (Fig. 9a) become completely white when visualized in high resolution (Fig. 9b). Therefore, propagation of these areas is now completed and sub-domains becomes consistent on a finer grid. In these regions, the consistency criterion is expected to rise when the mapping resolution increases.

4.1.2 Classification

Fig. 10 shows the results of the classification algorithm after two revolutions for the low-resolution mapping (left), the high-resolution mapping (middle), and from point-wise propagation using GRATIS (right). The latter used as a reference and derived through point-wise propagation from a sample of 10^5 points. Each color represents a different set, following the bridge between sets from DA to point-wise mapping established in Section 3.2. Thus, a set $\mathcal{A}$ from GRATIS classification is colored the same way as $\hat{\mathcal{A}}$ from DA classification. Since inconsistent sets $\hat{\mathcal{I}}_i$ and acrobatic sets $\mathcal{D}_i$ have not corresponding sets in point-wise and DA mappings, respectively, they share the same colors.

While these three mappings have a similar macroscopic look, they differ in many ways. First of all, the sizes of the inconsistent sets decrease dramatically from the low-resolution mapping to the high-resolution one. Moreover, these gains in consistency mainly benefit the representation of the stable set $\mathcal{W}_2$. Furthermore, the escape sets $\hat{\mathcal{X}}_1$ and $\hat{\mathcal{X}}_2$ are poorly mapped compared to the results of GRATIS on $\mathcal{X}_1$ and $\mathcal{X}_2$. These issues in the mapping are mostly due to errors in the approximation of the revolution period.
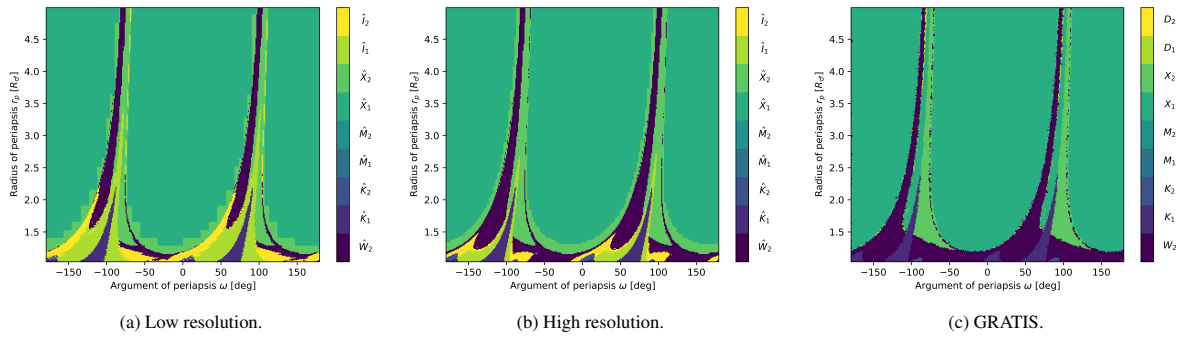
(a) Low resolution.   (b) High resolution.   (c) GRATIS.

Fig. 10: Results of the classification algorithm after 2 revolutions compared to GRATIS.

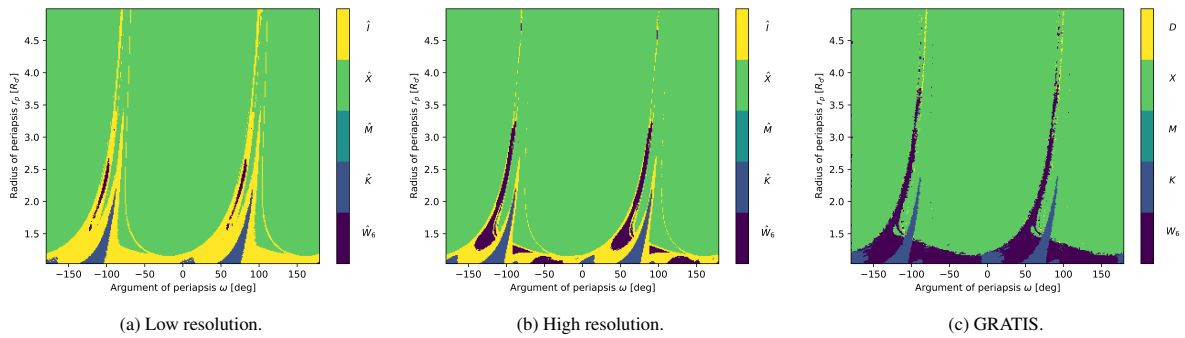(a) Low resolution.   (b) High resolution.   (c) GRATIS.

Fig. 11: Results of the classification algorithm after 6 revolutions compared to GRATIS.

Fig. 11 presents the results of the classification algorithm after six revolutions for the low-resolution mapping (left), the high-resolution mapping (middle), and from point-wise propagation using GRATIS (right). Also in this case the latter mapping is used as reference and it is derived through point-wise propagation from a sample of 10^5 points as before. These three charts show simplified mappings. For the sake of clarity, all sets $(\mathcal{A}_j)_{j\in[\![1,6]\!]}$ are united under the name $\mathcal{A}$, defined as

$$\mathcal{A} = \bigcup_{j=1}^{6} \mathcal{A}_j. \tag{9}$$

This representation method is adopted for all sets but $\mathcal{W}_6$, and $\hat{\mathcal{W}}_6$.

The same observations can be done for Figs. 10 and 11. However, Fig. 11 shows a strong predominance of the inconsistent set, especially at low resolution. The high-resolution mapping improves these results but still struggles to handle long accurate propagations on such a large search space. Nevertheless, these results show that DA mapping with ADS can highlight changes of behavior all over the search space. Moreover, DA mapping provides a continuous description of the domain. The dynamical behavior is the same everywhere, providing consistency. Meanwhile, point-wise computations deliver discrete information challenging to interpolate due to nonlinearities.

4.2 Quantitative performance analysis

After performing a qualitative analysis on the resulting DA mappings, the two criteria developed deliver quantitative data on the computed mappings.

4.2.1 Consistency criterion

In Fig. 12, the global consistency rate for both the low- and high-resolution mappings after several revolution periods are shown in bright and dark colors, respectively. The consistency at zero revolution is 100% since mappings only represent ICs. It appears that the consistency remains high, even after six revolutions, since it stays above 87%. It means that the size of the inconsistent sets is 13% or less on the total search space. Moreover, the consistency of the high-resolution mapping is around 5 points above the one of the low-resolution one. It demonstrates the gain of accuracy delivered by these additional computations.
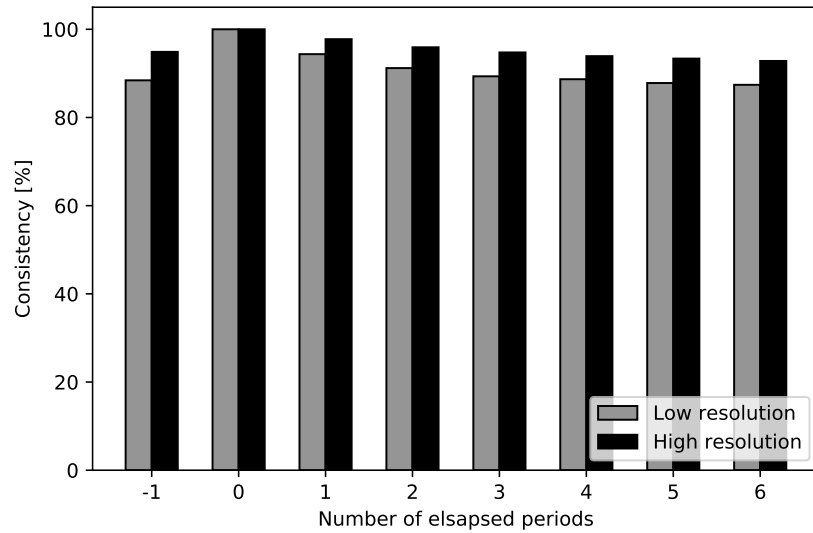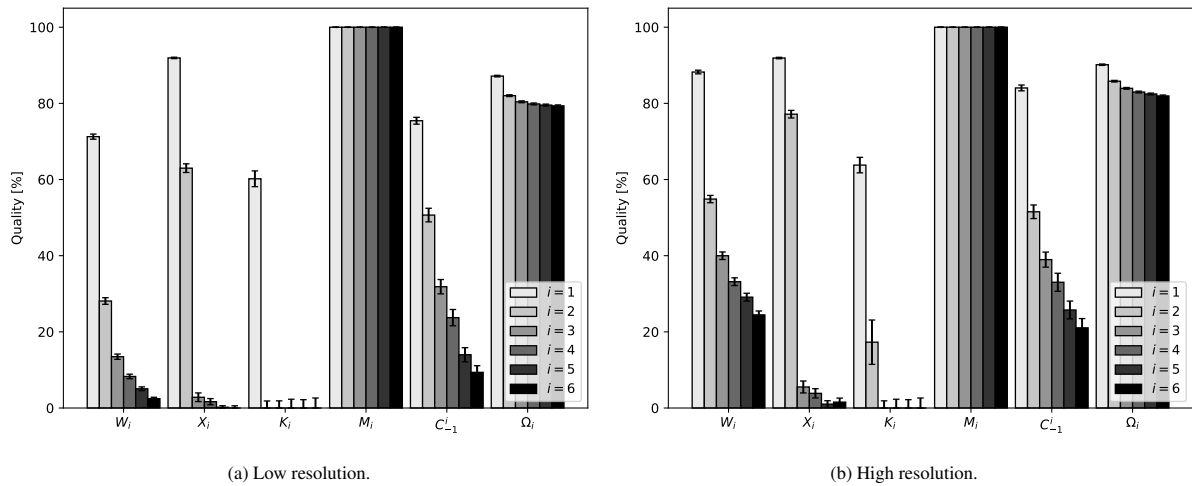
Fig. 12: Consistency criterion for several number of revolutions and the two mapping resolutions.

(a) Low resolution.

(b) High resolution.

Fig. 13: Quality criterion in percent of several sets and revolution periods. Note that Ω_i is used to refer to the quality criteria of Ω after i periods.

4.2.2 Quality criterion

Fig. 13 represents the quality criterion for both low- and high-resolution mappings on the left and right, respectively. Each group of bars corresponds to a different collection of sets. For instance, $\mathcal{X}_i$ for $i \in [\![1,6]\!]$. Differently, each color represents a different number of periods, from 1 (light) to 6 (dark). A bar's height represents the quality of that set in percent, while whiskers inform on the confidence interval at 95% on such value. These estimations of the quality criterion are computed against the sample of size 10^5 obtained with GRATIS.

The quality of acrobatic sets $\mathcal{D}_i$ is not shown since they are not mapped by the DA algorithm. In fact, their qualities are automatically set to 0%. In addition, the quality of moon-crash sets $\mathcal{M}_i$ is always 100%. Indeed, among the 10^5 propagated trajectories, none of them crashed on Mars' moons. The quality of these empty sets is then 100% by convention.

The quality criterion is always higher for the high-resolution mapping than for the low-resolution one. Especially for stable sets $\mathcal{W}_i$ and capture sets $\mathcal{C}^i_{-1}$ since a larger part of these sets becomes inconsistent during the low-resolution propagation, as shown by Fig. 11. Furthermore, capture sets $\mathcal{C}^i_{-1}$ are mapped in a better or equal way compared to stable sets $\mathcal{W}_i$. This is due to the positioning of $\mathcal{C}^i_{-1}$ farther from Mars (Merisio and Topputo, 2021), than most of $\mathcal{W}_i$. Thus, as highlighted in Figs. 10 and 11, the consistency of this region is higher, which enables better quality. However, designing a specific mission with ballistic capture requires much more data than these two criteria and is beyond the scope of this work. Moreover, this work does not provide any additional property on the identified solutions, except that they belong to capture sets.

Except for those two groups of sets, only slight improvements are remarkable when switching from low resolution to high resolution. Indeed, apart from $\mathcal{X}_1$, escape sets $\mathcal{X}_i$ and crash sets $\mathcal{K}_i$ fail to be accurately mapped, even though these regions of the search space are consistent. Indeed, the proposed classification algorithm does not track revolutions geometrically but uses period approximations. Consequently, the classification implies major approximations. Nevertheless, the poor mapping of these sets hardly impacts the quality of sets $\mathcal{W}_i$ due to their small sizes. Therefore, the global quality never drops below 80% in low resolution. The overall quality can be improved at a high computational cost, compared to the point-wise mapping, thanks to high-resolution mapping. Such a mapping improves the global classification results by at least 4. These poor performances are mainly due to the inability of the DA mapping engine to track revolutions geometrically instead of temporally. Thus, DA mapping as presented in this work cannot outperform point-wise mapping in terms of classification precision, but it exceeds point-wise mapping concerning computational cost.

5 Conclusion

This article presented a methodology to build cartography of ballistic capture sets using differential algebra mapping. It proposes an alternative classification algorithm to sort the sub-domains produced by the automatic domain splitting algorithm in newly defined capture sets. Moreover, instead of tracking revolutions with geometrical methods, as in Luo et al (2014), they are counted temporally, using regression on point-wise data. This work establishes a bridge between the point-wise mapping and DA mapping, allowing us to assess the performances of this new method. Hence, the introduction of two criteria. The first one is the consistency criterion, which represents the proportion of the search space where the mapping accuracy is guaranteed by the ADS algorithm. The second one is the quality criterion, which represents the success rate of the DA classification algorithm compared to the point-wise one.

Results show that DA mapping of BC sets could be performed on large search spaces, as ADS captured the dynamical variations on the whole domain. Furthermore, the consistency criterion shows that more than 87% of the search space is guaranteed by the ADS algorithm as accurate, even for low-resolution mappings. Moreover, the quality criterion demonstrates that the global error rate of DA mapping is below 20%. However, some small sets are either not or poorly mapped using revolution period regression, mainly due to the incapacity to count revolutions via geometrical information. This phenomenon does not disappear when the resolution of the mapping is increased. Nonetheless, DA mapping of BC sets can prove useful in various situations. For instance, it can be used for fast mapping of a plane, to then target a restricted domain of the search space. Either with a dense point-wise mapping or with a high-resolution DA mapping of the restricted area of interest.

References

Acton C (1996) Ancillary data services of NASA's navigation and ancillary information facility. Planetary and Space Science 44(1):65–70, doi:10.1016/0032-0633(95)00107-7

Acton C, Bachman N, Semenov B, Wright E (2018) A look towards the future in the handling of space science mission geometry. Planetary and Space Science 150:9–12, doi:10.1016/j.pss.2017.02.013

Aguiar G, Topputo F (2018) A technique for designing Earth–Mars low-thrust transfers culminating in ballistic capture. In: 7th International Conference on Astrodynamics Tools and Techniques (ICATT), pp 1–8

Archinal B, A'Hearn M, Bowell E, Conrad A, Consolmagno G, Courtin R, Fukushima T, Hestroffer D, Hilton J, Krasinsky G, et al (2011) Report of the IAU working group on cartographic coordinates and rotational elements: 2009. Celestial Mechanics and Dynamical Astronomy 109(2):101–135, doi:10.1007/s10569-010-9320-4

Armellin R, Di Lizia P, Bernelli-Zazzera F, Berz M (2010) Asteroid close encounters characterization using differential algebra: the case of Apophis. Celestial Mechanics and Dynamical Astronomy 107(4):451–470, doi:10.1007/s10569-010-9283-5

Baresi N, Fu X, Armellin R (2021) A high-order taylor polynomials approach for continuing trajectories in restricted three-body problems. In: 2020 AAS/AIAA Astrodynamics Specialist Conference (South Lake Tahoe, California), 09/08/2020 - 13/08/2020), pp 1–19

---

[1] `https://zenodo.org/` [last accessed Feb 1, 2022]

Belbruno E (1987) Lunar capture orbits, a method of constructing Earth Moon trajectories and the lunar GAS mission. In: 19th International Electric Propulsion Conference, American Institute of Aeronautics and Astronautics, pp 1–9, doi:10.2514/6.1987-1054

Belbruno E (2004) Capture Dynamics and Chaotic Motions in Celestial Mechanics. Princeton University Press, doi:10.1515/9780691186436

Belbruno E (2020) Relation between solutions of the Schrödinger equation with transitioning resonance solutions of the gravitational three-body problem. Journal of Physics Communications 4(1):015,012, doi:10.1088/2399-6528/ab693f

Belbruno E, Carrico J (2000) Calculation of weak stability boundary ballistic lunar transfer trajectories. In: Astrodynamics Specialist Conference, p 4142, doi:10.2514/6.2000-4142

Belbruno E, Miller J (1990) A ballistic lunar capture trajectory for the Japanese spacecraft Hiten. Tech. rep., Jet Propulsion Laboratory, IOM 312/904-1731-EAB

Belbruno E, Miller J (1993) Sun-perturbed Earth-to-Moon transfers with ballistic capture. Journal of Guidance, Control, and Dynamics 16(4):770–775, doi:10.2514/3.21079

Belbruno E, Topputo F, Gidea M (2008) Resonance transitions associated to weak capture in the restricted three-body problem. Advances in Space Research 42(8):1330–1351, doi:10.1016/j.asr.2008.01.018

Belbruno E, Gidea M, Topputo F (2010) Weak stability boundary and invariant manifolds. SIAM Journal on Applied Dynamical Systems 9(3):1061–1089, doi:10.1137/090780638

Belbruno E, Gidea M, Topputo F (2013) Geometry of weak stability boundaries. Qualitative Theory of Dynamical Systems 12(1):53–66, doi:10.1007/s12346-012-0069-x

Benkhoff J, Murakami G, Baumjohann W, Besse S, Bunce E, Casale M, Cremonese G, Glassmeier K-H, Hayakawa H, Heyner D, et al (2021) BepiColombo-mission overview and science goals. Space Science Reviews 217(8):1–56, doi:10.1007/s11214-021-00861-4

Berz M (1992) High-order computation and normal form analysis of repetitive systems. In: AIP Conference Proceedings, pp 1–36, doi:10.1063/1.41975

Berz M (1999) Modern Map Methods in Particle Beam Physics. Elsevier, doi:10.1016/s1076-5670(08)70227-1

Caleb T, Lizy-Destrez S (2021) Can uncertainty propagation solve the mysterious case of Snoopy? In: Vasile M, Quagliarella D (eds) Advances in Uncertainty Quantification and Optimization Under Uncertainty with Aerospace Applications, Springer International Publishing, pp 109–128, doi:10.1007/978-3-030-80542-5_8

Chung M, Hatch S, Kangas J, Long S, Roncoli R, Sweetser T (2010) Trans-lunar cruise trajectory design of GRAIL (Gravity Recovery and Interior Laboratory) mission. In: AIAA/AAS Astrodynamics Specialist Conference, p 8384, doi:10.2514/6.2010-8384

Circi C, Teofilatto P (2001) On the dynamics of weak stability boundary lunar transfers. Celestial Mechanics and Dynamical Astronomy 79(1):41–72, doi:10.1023/A:1011153610564

Dei Tos D, Russell R, Topputo F (2018) Survey of Mars ballistic capture trajectories using periodic orbits as generating mechanisms. Journal of Guidance, Control, and Dynamics 41(6):1227–1242, doi:10.2514/1.g003158

Di Lizia Pierluigi, Armellin R, Lavagna M (2008) Application of high order expansions of two-point boundary value problems to astrodynamics. Celestial Mechanics and Dynamical Astronomy 102(4):355–375, doi:10.1007/s10569-008-9170-5

García F, Gómez G (2007) A note on weak stability boundaries. Celestial Mechanics and Dynamical Astronomy 97(2):87–100, doi:10.1007/s10569-006-9053-6

Hairer E, Nørsett S, Wanner G (1993) Solving Ordinary Differential Equations I. Springer Berlin Heidelberg, doi:10.1007/978-3-540-78862-1

Haller G (2011) A variational theory of hyperbolic lagrangian coherent structures. Physica D: Nonlinear Phenomena 240(7):574–598, doi:10.1016/j.physd.2010.11.010

Hanley J, Lippman-Hand A (1983) If nothing goes wrong, is everything all right? Journal of American Medical Association (JAMA) 249(13):1743, doi:10.1001/jama.1983.03330370053031

Hyeraci N, Topputo F (2010) Method to design ballistic capture in the elliptic restricted three-body problem. Journal of guidance, control, and dynamics 33(6):1814–1823, doi:10.2514/1.49263

Ivashkin V (2002) On trajectories of Earth–Moon flight of a particle with its temporary capture by the Moon. In: Doklady Physics, Springer, vol 47, pp 825–827, doi:10.1134/1.1526433

Luo Z-F, Topputo F (2015) Analysis of ballistic capture in Sun–planet models. Advances in Space Research 56(6):1030–1041, doi:10.1016/j.asr.2015.05.042

Luo Z-F, Topputo F (2017) Capability of satellite-aided ballistic capture. Communications in Nonlinear Science and Numerical Simulation 48:211–223, doi:10.1016/j.cnsns.2016.12.021

Luo Z-F, Topputo F (2021) Mars orbit insertion via ballistic capture and aerobraking. Astrodynamics 5(2):167–181, doi:10.1007/s42064-020-0095-4

Luo Z-F, Topputo F, Bernelli-Zazzera F, Tang G (2014) Constructing ballistic capture orbits in the real Solar System model. Celestial Mechanics and Dynamical Astronomy 120(4):433–450, doi:10.1007/s10569-014-9580-5

Manzi M, Topputo F (2021) A flow-informed strategy for ballistic capture orbit generation. Celestial Mechanics and Dynamical Astronomy 133(11-12):1–16, doi:10.1007/s10569-021-10048-2

Massari M, Di Lizia P, Cavenago F, Wittig A (2018) Differential algebra software library with automatic code generation for space embedded applications. In: 2018 AIAA Information Systems-AIAA Infotech @ Aerospace, American Institute of Aeronautics and Astronautics, pp 1–13, doi:10.2514/6.2018-0398

Merisio G, Topputo F (2021) Characterization of ballistic capture corridors aiming at autonomous ballistic capture at Mars. In: 2021 AIAA/AAS Astrodynamics Specialist Conference, pp 1–21

Montenbruck O, Gill E (2000) Satellite Orbits Models, Methods and Applications. Springer, doi:10.1007/978-3-642-58351-3

Park R, Folkner W, Williams J, Boggs D (2021) The JPL planetary and lunar ephemerides DE440 and DE441. The Astronomical Journal 161(3):105, doi:10.3847/1538-3881/abd414

Pirovano L, Armellin R, Siminski J, Flohrer T (2021) Differential algebra enabled multi-target tracking for too-short arcs. Acta Astronautica 182:310–324, doi:10.1016/j.actaastro.2021.02.023

Prince P, Dormand J (1981) High order embedded Runge-Kutta formulae. Journal of computational and applied mathematics 7(1):67–75, doi:10.1016/0771-050x(81)90010-3

Racca G, Marini A, Stagnaro L, Van Dooren J, Di Napoli L, Foing B, Lumb R, Volp J, Brinkmann J, Grünagel R, et al (2002) SMART-1 mission description and development status. Planetary and space science 50(14-15):1323–1337, doi:10.1016/S0032-0633(02)00123-X

Rasotto M, Morselli A, Wittig A, Massari M, Di Lizia P, Armellin R, Yabar Valles C, Urbina Ortega C (2016) Differential algebra space toolbox for nonlinear uncertainty propagation in space dynamics. In: 6th International Conference on Astrodynamics Tools and Techniques (ICATT), International Conference on Astrodynamics Tools and Techniques, pp 1–11

Robert C, Casella G (2004) Monte Carlo Statistical Methods. Springer New York, doi:10.1007/978-1-4757-4145-2

Scheeres D, Rosengren A, McMahon J (2011) The dynamics of high area-to-mass ratio objects in earth orbit: The effect of solar radiation pressure. In: Proceedings of the AAS/AIAA Space Flight Mechanics Meeting, number AAS, pp 11–178

Schuster A, Jehn R (2014) Influence of the Mercury gravity field on the orbit insertion strategy of BepiColombo. Aerospace Science and Technology 39:546–551, doi:10.1016/j.ast.2014.06.003

Servadio S, Zanetti R (2021) Differential algebra-based multiple Gaussian particle filter for orbit determination. Journal of Optimization Theory and Applications 191:1–27, doi:10.1007/s10957-021-01934-8

Servadio S, Zanetti R, Armellin R (2022) Maximum a posteriori estimation of Hamiltonian systems with high order Taylor polynomials. The Journal of the Astronautical Sciences 69(2):511–536, doi:10.1007/s40295-022-00304-4

Sousa Silva P, Terra M (2012) Applicability and dynamical characterization of the associated sets of the algorithmic weak stability boundary in the lunar sphere of influence. Celestial Mechanics and Dynamical Astronomy 113(2):141–168, doi:10.1007/s10569-012-9409-z

Topputo F, Belbruno E (2009) Computation of weak stability boundaries: Sun–Jupiter system. Celestial Mechanics and Dynamical Astronomy 105(1-3):3–17, doi:10.1007/s10569-009-9222-5

Topputo F, Belbruno E (2015) Earth–Mars transfers with ballistic capture. Celestial Mechanics and Dynamical Astronomy 121(4):329–346, doi:10.1007/s10569-015-9605-8

Topputo F, Belbruno E, Gidea M (2008) Resonant motion, ballistic escape, and their applications in astrodynamics. Advances in Space Research 42(8):1318–1329, doi:10.1016/j.asr.2008.01.017

Topputo F, Dei Tos D, Mani K, Ceccherini S, Giordano C, Franzese V, Wang Y (2018) Trajectory design in high-fidelity models. In: 7th International Conference on Astrodynamics Tools and Techniques (ICATT), pp 1–9

Topputo F, Wang Y, Giordano C, Franzese V, Goldberg H, Perez-Lissi F, Walker R (2021) Envelop of reachable asteroids by M-ARGO CubeSat. Advances in Space Research 67(12):4193–4221, doi:10.1016/j.asr.2021.02.031

Valli M, Armellin R, Di Lizia P, Lavagna M (2013) Nonlinear mapping of uncertainties in celestial mechanics. Journal of Guidance, Control, and Dynamics 36(1):48–63, doi:10.2514/1.58068

Wittig A, Di Lizia P, Armellin R, Makino K, Bernelli-Zazzera F, Berz M (2015) Propagation of large uncertainty sets in orbital dynamics by automatic domain splitting. Celestial Mechanics and Dynamical Astronomy 122(3):239–261, doi:10.1007/s10569-015-9618-3

Wittig A, Colombo C, Armellin R (2017) Long-term density evolution through semi-analytical and differential algebra techniques. Celestial Mechanics and Dynamical Astronomy 128(4):435–452, doi:10.1007/s10569-017-9756-x